Coulomb excitation of ^{80,82}Kr and a change in structure approaching $N = Z = 40$

S. A. Gillespie,[1,*] J. Henderson ![ORCID],[2,3,†] K. Abrahams,[4] F. A. Ali,[5,6] L. Atar,[5] G. C. Ball,[1] N. Bernier,[1,7,‡] S. S. Bhattcharjee,[1,§]
R. Caballero-Folch,[1] M. Bowry,[1] A. Chester,[1,∥] R. Coleman,[5] T. Drake,[8] E. Dunling,[1,9] A. B. Garnsworthy,[1] B. Greaves,[5]
G. F. Grinyer,[10] G. Hackman,[1] E. Kasanda,[5] R. LaFleur,[1] S. Masango,[4] D. Muecher,[5] C. Ngwetsheni,[4] S. S. Ntshangase,[11]
B. Olaizola,[1,¶] J. N. Orce,[4] T. Rockman,[5] Y. Saito,[1,7] L. Sexton,[1,2] P. Šiurytė,[1,2] J. Smallcombe,[1,#] J. K. Smith,[12,**]
C. E. Svensson,[5] E. Timakova,[1] R. Wadsworth,[9] J. Williams,[13,††] M. S. C. Winokan,[1] C. Y. Wu,[3] and T. Zidar[5]

[1]*TRIUMF, Vancouver, British Columbia V6T 2A3, Canada*
[2]*Department of Physics, University of Surrey, Guildford GU2 7XH, United Kingdom*
[3]*Lawrence Livermore National Laboratory, Livermore, California 94550, USA*
[4]*Department of Physics and Astronomy, University of the Western Cape, P/B X17, Bellville, ZA-7535, South Africa*
[5]*Department of Physics, University of Guelph, Guelph, ON N1G 2W1, Canada*
[6]*Department of Physics, College of Education, University of Sulaimani, P.O. Box 334, Sulaimani, Kurdistan Region, Iraq*
[7]*Department of Physics and Astronomy, University of British Columbia, Vancouver V6T 1Z1, Canada*
[8]*Department of Physics, University of Toronto, Toronto, Ontario M5S 1A7, Canada*
[9]*Department of Physics, University of York, Heslington, York YO10 5DD, UK*
[10]*Department of Physics, University of Regina, Saskatchewan S4S 0A2, Canada*
[11]*Physics Department, University of Zululand, Private Bag X1001, KwaDlangezwa 3886, South Africa*
[12]*Physics Department, Reed College, Portland, Oregon 97202, USA*
[13]*Simon Fraser University, 8888 University Drive, Burnaby, British Columbia V5A 1S6, Canada*

Background: Nuclei approaching $N = Z = 40$ are known to exhibit strongly deformed structures and are thought to be candidates for shape coexistence. In the krypton isotopes, ^{80,82}Kr are poorly characterized, preventing an understanding of evolving deformation approaching $N = 40$.

Purpose: The present work aims to determine electric quadrupole transition strengths and quadrupole moments of ^{80,82}Kr in order to better characterize their deformation.

Methods: Sub-barrier Coulomb excitation was employed, impinging the isotopes of krypton on ^{196}Pt and ^{208}Pb targets. Utilizing a semiclassical description of the safe Coulomb-excitation process $E2$ matrix elements could then be determined.

Results: Eleven new or improved matrix elements are determined in ^{80}Kr and seven in ^{82}Kr. The new $B(E2; 0_1^+ \rightarrow 2_1^+)$ value in ^{82}Kr disagrees with the evaluated value by 3σ, which can be explained in terms of deficiencies in a previous Coulomb-excitation analysis.

Conclusions: Comparison of measured $Q_s(2_1^+)$ and $B(E2; 0_1^+ \rightarrow 2_1^+)$ values indicates that neutron-deficient ($N \leqslant 42$) isotopes of krypton are closer to axial deformation than other isotopic chains in the mass region. A continuation of this trend to higher Z may result in Sr and Zr isotopes exhibiting near-axial prolate deformation.

I. INTRODUCTION

Deformation is an ever-present feature of atomic nuclei, arising even in doubly magic systems that might traditionally be considered spherical [1]. Dramatic changes in deformation across isotopic and isotonic chains is often symptomatic of a change in the underlying microscopic configuration. The region around $N = Z = 40$ lies in what might nominally be

---

*stephen.gillespie.90@gmail.com; Present address: National Superconducting Cyclotron Laboratory, Michigan State University, East Lansing, Michigan 48824, USA

†jack.henderson@surrey.ac.uk

‡Present address: Department of Physics and Astronomy, University of the Western Cape, P/B X17, Bellville, ZA-7535, South Africa

§Present address: Institute of Experimental and Applied Physics, Czech Technical University in Prague, Husova 240/5, 110 00 Prague 1, Czech Republic

∥Present address: National Superconducting Cyclotron Laboratory, Michigan State University, East Lansing, Michigan 48824, USA

¶ISOLDE-EP, CERN, CH-1211 Geneva 23, Switzerland

#Present address: Oliver Lodge Laboratory, University of Liverpool, Liverpool L69 7ZE, United Kingdom

**Present address: Department of Physics and Astronomy, Northwestern University, Evanston, Illinois 60208, USA

††Present address: TRIUMF, Vancouver, BC V6T 2A3, Canada

expected to be a near-spherical region, with the nucleon number 40 being a subshell closure. Experimental work, however, has demonstrated that the region instead exhibits an exceptional degree of quadrupole deformation (see, e.g., Ref. [2]). The picture is further complicated by the predicted existence of multiple competing nuclear configurations, as highlighted in a theoretical study of the $N = Z = 40$ nucleus, ^{80}Zr [3], in which multiple shape-coexistence was predicted.

Regions of the nuclear landscape in which markedly different configurations are near degenerate in energy provide a challenging testing ground for nuclear theory, requiring precise determinations of their relative energies. Typically, such different configurations are associated with different macroscopic shapes, giving rise to the phenomenon of shape coexistence. It is convenient to consider the different configurations in terms of their respective deformation, as these give rise to experimentally observable quantities such as electric quadrupole transition strengths and moments that can be directly compared to theoretical predictions.

Neutron-deficient isotopes of krypton have been experimentally associated with both strongly deformed structures and shape coexistence, evidenced by low-lying excited 0^+ states and supported by Coulomb-excitation measurements. For example, Coulomb-excitation measurements of radioactive ^{74,76}Kr, performed by Clement *et al.* [4], indicate a near-axial prolate ground state coexisting with a largely triaxial configuration. Measurements of stable ^{78}Kr [5,6] support this picture of a near axially deformed prolate ground state and a triaxial coexisting configuration.

In heavier isotopes of krypton, however, experimental data are lacking. In particular, spectroscopic quadrupole moments of 2_1^+ states $[Q_s(2_1^+)]$ have not been experimentally determined in either of ^{80}Kr or ^{82}Kr. These observables provide the clearest metric of a nuclear shape and are thus an essential ingredient in a systematic study of the isotopic chain. In the present work we present Coulomb-excitation measurements of both of these isotopes on high-Z targets, providing the first experimental determination of $Q_s(2_1^+)$ in both cases. Through comparison of the present results with measured values in lighter isotopes of krypton and isotones of selenium and germanium, we are able to demonstrate a shift towards centrally axial deformation approaching $N = Z = 40$.

II. EXPERIMENT AND ANALYSIS

Beams of ^{80,82}Kr were provided by the TRIUMF offline ion source (OLIS) [7], injected into the ISAC accelerator chain and accelerated to energies of 4.17 MeV/u, corresponding to about 71% of the Coulomb-barrier height. The beams were impinged upon a self-supporting 1.5 mg/cm^2 ^{196}Pt target and a 1 mg/cm^2 ^{208}Pb target, where the ^{208}Pb target was backed with a 40 μg/cm^2 carbon foil. Two micron S3-type [8] double-sided silicon strip detectors were mounted in the BAMBINO chamber and used to detect scattered beam- and target-like nuclei, with one detector located downstream of the target and one upstream. The target chamber was surrounded by fourteen detectors of the TRIUMF-ISAC gamma-ray escape-suppressed spectrometer (TIGRESS) [9] for the detection of γ rays emitted in the de-excitation of
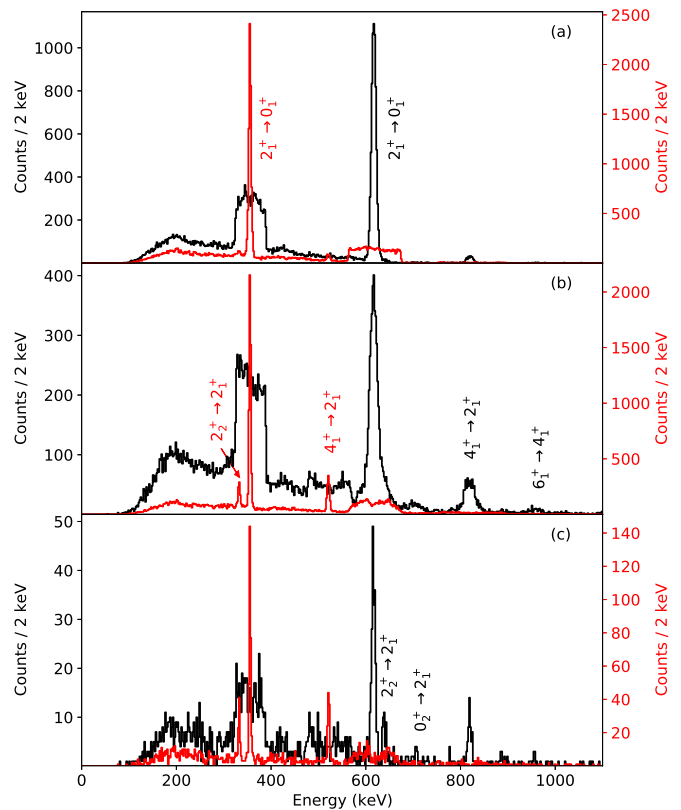

FIG. 1. Doppler corrected TIGRESS-S3 coincidence spectra in the beam (^{80}Kr, black) and target (^{196}Pt, red) frame for: (a) Beam-like nuclei scattered and detected in the downstream S3 detector. (b) Target-like nuclei scattered and detected in the downstream S3 detector. (c) Beam-like nuclei scattered and detected in the upstream S3 detector. Transitions relevant to the present work are indicated. Note that the resolution for beam-like γ rays identified in coincidence with target-like scattered ions is worsened due to the slowing of the beam-like recoil within the target.

the nuclei of interest. The TIGRESS clover detectors were arranged in a Compton-suppressed configuration, with the fronts of the detectors 145 mm from the target position. Beam intensities of approximately 1×10^6 pps were maintained for approximately 7 and 4 h for ^{80}Kr and ^{82}Kr, respectively.

Data were analyzed using the GRSISort analysis package [10], written in a ROOT framework [11]. Silicon pixels were constructed using energy- and time-coincident conditions, with coincident γ rays in TIGRESS selected on the basis of a ± 100 ns time-coincidence. γ-ray events were added-back to enhance detection efficiency. γ-ray energies were then Doppler-corrected on the basis of the reaction kinematics as determined from the measured particle scattering angle determined in the silicon detectors and the γ-ray emission angle determined from the subcrystal electronic-segmentation of the TIGRESS clover detectors. Example Doppler-corrected γ-ray spectra are shown in Figs. 1 and 2 for ^{80}Kr and ^{82}Kr, respectively. Reduced level schemes showing the levels and transitions observed in the present work are shown in Fig. 3.

Scattered beam- and target-like particle detections were subdivided into angular bins corresponding to a near-
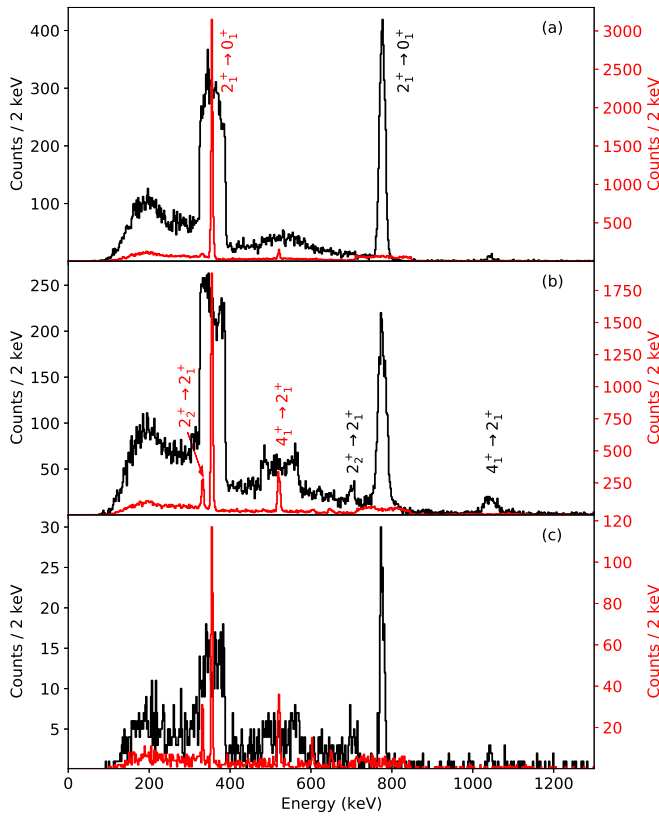
FIG. 2. Doppler corrected TIGRESS-S3 coincidence spectra in the beam (^{82}Kr, black) and target (^{196}Pt, red) frame for: (a) Beam-like nuclei scattered and detected in the downstream S3 detector. (b) Target-like nuclei scattered and detected in the downstream S3 detector. (c) Beam-like nuclei scattered and detected in the upstream S3 detector. Transitions relevant to the present work are indicated.

FIG. 3. Levels and transitions relevant to the present work for (a) ^{80}Kr and (b) ^{82}Kr.

continuous coverage of center-of-mass angles between 27° and 167° with respect to the beam axis. γ-ray detection efficiencies were determined with ^{60}Co, ^{152}Eu, and ^{133}Ba sources. γ-ray yields were then efficiency corrected, allowing for comparison with those calculated using the GOSIA [12] coupled-channels semiclassical Coulomb-excitation code. Upstream detections correspond to a minimum separation smaller than the empirical 5 fm required for safe Coulomb excitation and were therefore excluded from the Coulomb-excitation analysis. However these data still provided useful useful information on the state population due to the typically superior γ-ray energy resolution as shown in the bottom panels of Figs. 1 and 2.

Coulomb-excitation yields were calculated with GOSIA and were fitted to the experimental data with the MINUIT [13] package of minimization tools, using the MIGRAD algorithm. Data from ^{196}Pt were used to provide a target normalization, providing sensitivity to absolute matrix elements in the krypton isotopes. Matrix elements of ^{196}Pt used in the normalization procedure are shown in Table I. Literature $E2/M1$ mixing ratios (δ) and branching ratios for ^{80,82}Kr were used to further constrain the fits, where available, and are given in Table II. Full covariances could be extracted from the mini-
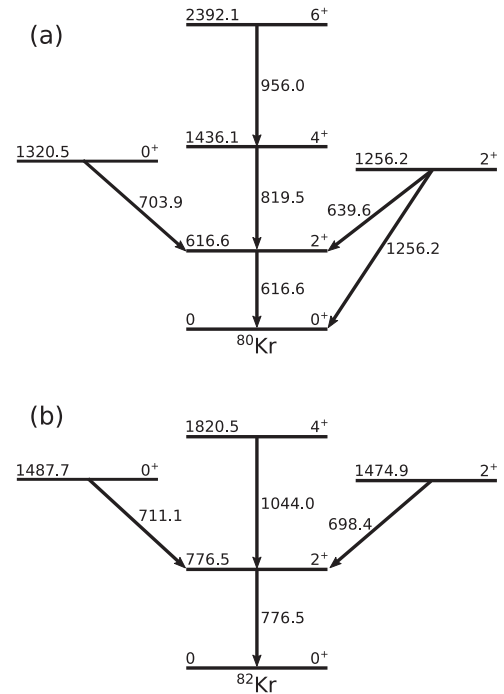
mization, which allowed for comparison with the χ^2 surface scan method described in Ref. [14], in which an iterative process is used. Central values and uncertainties were found to be consistent with the present method and the iterative technique of Ref. [14]. Covariances and correlations extracted from the minimization are reported in the Appendix of the present

TABLE I. Matrix elements for ^{196}Pt used to constrain the present analysis. The stated krypton isotope indicates whether the matrix element was allowed to vary in the minimization and contribute to the χ^2. For example, the $\langle 2_1^+ | E2 | 2_2^+ \rangle$ matrix element was permitted to vary during the ^{80}Kr analysis and its discrepancy from literature contributed to the χ^2 value. In the ^{82}Kr analysis, on the other hand, the matrix element was fixed and its influence on the determined matrix elements was investigated by repeating the minimization procedure at the $\pm\sigma$ limits.

i	f	$\langle J_i^\pi | E2 | J_f^\pi \rangle$ $(e^2 \mathrm{b}^2)$	Notes	Ref.
0_1^+	2_1^+	1.172(5)	^{80,82}Kr	[15]
2_1^+	2_1^+	0.82(10)	^{80,82}Kr	[16]
2_1^+	2_2^+	1.36(1)	^{80,82}Kr	[16]
2_1^+	4_1^+	1.91(2)	^{80,82}Kr	[16]
2_1^+	0_2^+	0.167(15)	^{80}Kr	[16]
2_2^+	2_2^+	−0.52(20)	^{80}Kr	[16]
2_2^+	0_2^+	−0.35(70)	^{80}Kr	[16]
4_1^+	4_1^+	1.36(16)	^{80}Kr	[16]
i	f	$\langle J_i^\pi | M1 | J_f^\pi \rangle$ (μ_N)	Notes	
2_1^+	2_2^+	0.0723(64)	^{80,82}Kr	[15]

TABLE II. Literature branching ratios (BR) and mixing ratios (δ) used to constrain the GOSIA minimization. Data were taken from ENSDF [15] with the exception of the ^{80}Kr BR, which was taken from Ref. [17].

^{80}Kr

i	f_1	f_2	BR$\left[\frac{i \to f_1}{i \to f_2}\right]$
2^+_2	0^+_1	2^+_1	0.331(4)
$i \to f$	δ		
$2^+_2 \to 2^+_1$	6(1)		

^{82}Kr

i	f_1	f_2	BR$\left[\frac{i \to f_1}{i \to f_2}\right]$
2^+_2	0^+_1	2^+_1	0.577(6)
$i \to f$	δ		
$2^+_2 \to 2^+_1$	2.1(4)		

work. The method used here allowed for the simultaneous fitting of the ^{208}Pb and ^{196}Pt data, improving uncertainties due to enhanced sensitivity to strongly correlated matrix elements. The matrix elements of ^{196}Pt (indicated in Table I by the corresponding krypton isotope) were permitted to vary and contribute to the χ^2 during the minimization procedure.

Figure 4 shows the consistent confidence intervals extracted from the method used here compared with the χ^2 surface scan method described in Ref. [14] for ^{80}Kr, varying
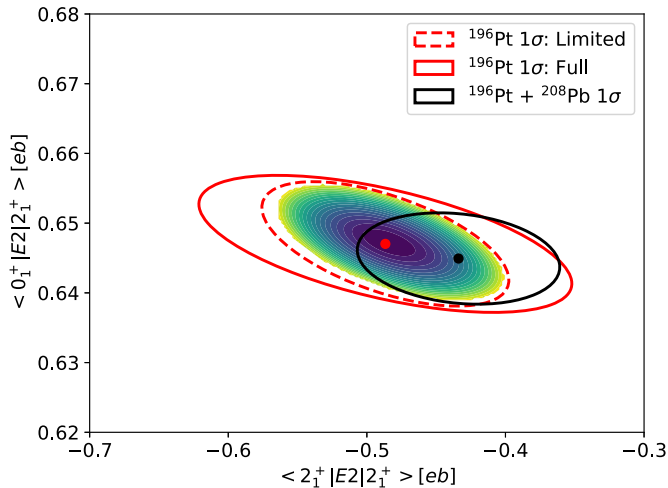

FIG. 4. Confidence intervals for the $\langle 0^+_1 | E2 | 2^+_1 \rangle$ and $\langle 2^+_1 | E2 | 2^+_1 \rangle$ matrix elements in ^{80}Kr, calculated using the fitting technique described in the text. Filled points correspond to the $\chi^2 + 1$ distribution calculated from a two-dimensional scan [14]. The dashed red ellipse ("limited") is the corresponding 1σ confidence interval using the MINUIT method described here, where only the $\langle 0^+_1 | E2 | 2^+_1 \rangle$ and $\langle 2^+_1 | E2 | 2^+_1 \rangle$ matrix elements were permitted to vary. The solid ellipses correspond to confidence intervals from a minimization in which all relevant matrix elements were allowed to vary. The two solid ellipses correspond to minimisations using only the ^{196}Pt data (red) and the complete data set, incorporating both ^{196}Pt and ^{208}Pb data (black). The points correspond to the central values obtained from the MINUIT method.
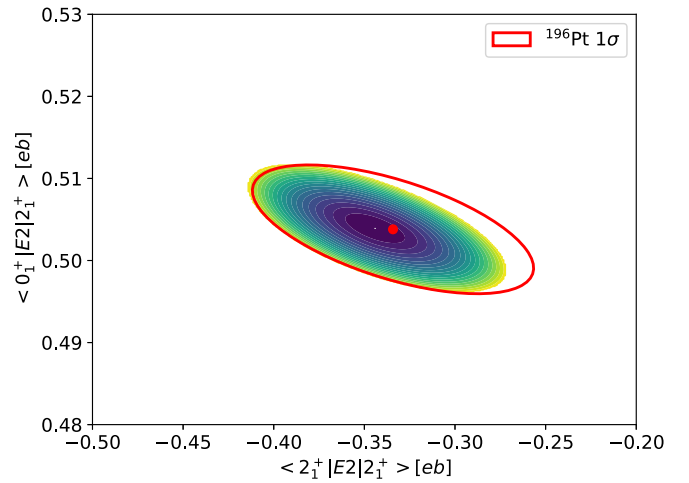

FIG. 5. Confidence intervals for the $\langle 0^+_1 | E2 | 2^+_1 \rangle$ and $\langle 2^+_1 | E2 | 2^+_1 \rangle$ matrix elements in ^{82}Kr, calculated using the fitting techniques described in the text. As near-identical confidence intervals are obtained from the limited and full analysis when compared to Fig. 4 only the confidence limit from the full minimization is shown. This results from the fact that other matrix elements included in the full minimization are not strongly correlated with $\langle 2^+_1 | E2 | 2^+_1 \rangle$. The point corresponds to the central value from the MINUIT minimization.

only the $\langle 0^+_1 | E2 | 2^+_1 \rangle$ and $\langle 2^+_1 | E2 | 2^+_1 \rangle$ matrix elements. Also shown are the intervals for full minimisations (i.e., all relevant matrix elements allowed to vary) using the ^{196}Pt data, and the combined ^{196}Pt and ^{208}Pb data. Figure 5 shows the same for ^{82}Kr. In the ^{82}Kr case only a single confidence interval is shown, as the intervals for the limited and full minimization are near-identical. This because, in the ^{82}Kr analysis, those matrix elements that are strongly correlated with the diagonal matrix element, $\langle 2^+_1 | E2 | 2^+_1 \rangle$, and are included in the minimisation are well constrained in the fit. Other strongly correlated matrix elements are kept fixed due to there being no experimental data with which they can be constrained and the fact that their inclusion in the minimization prevents convergence. In ^{80}Kr, on the other hand, a much broader fit is performed due to the more extensive data, resulting in a number of less well-constrained matrix elements contributing to the uncertainty in $\langle 2^+_1 | E2 | 2^+_1 \rangle$. To account for this, matrix elements that prevented convergence and so could not be included during the minimization were varied and used to estimate a systematic uncertainty. For example, the poorly constrained $\langle 2^+_1 | E2 | 0^+_2 \rangle$ matrix element is a significant source of systematic uncertainty for the $\langle 2^+_1 | E2 | 2^+_1 \rangle$ matrix element in ^{82}Kr.

III. DISCUSSION

All matrix elements determined in the present work are summarized in Tables III and IV for ^{80}Kr and ^{82}Kr, respectively. Also shown are literature data where available. Systematic uncertainties correspond to contributions from matrix elements not varied in the minimization routine as discussed previously, which are quoted when significant.

We note that the $\langle 0^+_1 | E2 | 2^+_1 \rangle$ matrix element in ^{82}Kr in this work [and hence the $B(E2; 0^+_1 \to 2^+_1)$ value] disagrees

TABLE III. Matrix elements for ^{80}Kr as determined in the present work, compared to literature data, where available. Systematic uncertainties, where significant, are quoted as a second uncertainty.

	This work		Literature		
^{80}Kr					
$J_i^\pi \to J_f^\pi$	$\langle J_i^\pi \| E2 \| J_f^\pi \rangle$ [eb]	$B(E2; J_i^\pi \to J_f^\pi)$ [e^2fm^4]	$\langle J_i^\pi \| E2 \| J_f^\pi \rangle$ [eb]	$B(E2; J_i^\pi \to J_f^\pi)$ [e^2fm^4]	Reference
$0_1^+ \to 2_1^+$	0.645(7)	4159(84)	$0.618\binom{20}{18}$	$3825\binom{250}{225}$	[15]
			$0.618\binom{28}{25}$	$3825\binom{350}{300}$	[18]
			$0.608\binom{16}{17}$	3700(200)	[19]
			$0.638\binom{22}{19}$	$4070\binom{280}{245}$	[20]
$0_1^+ \to 2_2^+$	0.078(15)	61(23)	$0.055\binom{6}{7}$	30(7)	[15]
$2_1^+ \to 2_2^+$	0.73(14)	1074(406)	0.51(4)	512(73)	[15]
$2_1^+ \to 0_2^+$	0.33(12)	223(155)			
$2_1^+ \to 4_1^+$	1.069(30)	2287(130)	$1.135\binom{44}{46}$	2575(204)	[15]
			$0.927\binom{144}{124}$	$1720\binom{575}{340}$	[18]
			$0.900\binom{57}{51}$	$1620\binom{210}{180}$	[19]
			$1.135\binom{44}{46}$	2575(204)	[20]
$2_2^+ \to 0_1^+$	$-0.08(63)$	14(180)			[a]
$4_1^+ \to 6_1^+$	1.68(12)	3140(430)			
$J_i^\pi \to J_f^\pi$	$\langle J_i^\pi \| M1 \| J_f^\pi \rangle$ [μ_N]	$B(M1; J_i^\pi \to J_f^\pi)$ [μ_N^2]	$\langle J_i^\pi \| M1 \| J_f^\pi \rangle$ [μ_N]	$B(M1; J_i^\pi \to J_f^\pi)$ [μ_N^2]	Reference
$2_1^+ \to 2_2^+$	0.065(16)	0.00085(39)	0.045(8)	0.00041(16)	[15]
	$\langle J_i^\pi \| E2 \| J_i^\pi \rangle$ [eb]	$Q_s(J^\pi)$ [$e$fm^2]	$\langle J_i^\pi \| E2 \| J_i^\pi \rangle$ [eb]	$Q_s(J^\pi)$ [$e$fm^2]	Reference
2_1^+	$-0.43(7)$	$-33(6)$			
2_2^+	0.4(17)	34(126)			
4_1^+	$-0.77(22)$	$-58(16)$			

[a]Transition not observed.

with that in the literature [15], at the level of about 3σ. The evaluated value for this matrix element is taken from an earlier Coulomb-excitation study [21]. In that work a value of $Q_s(2_1^+) = 0$ was assumed, based on interacting boson approximation calculations. The discrepancy in $B(E2; 0_1^+ \to 2_1^+)$ can thus be explained by the significant correlation between the $\langle 2_1^+ | E2 | 2_1^+ \rangle$ and $\langle 0_1^+ | E2 | 2_1^+ \rangle$ matrix elements and the observed $Q_s(2_1^+)$ value, found to be large and negative. Indeed, by enforcing the same constraint on $Q_s(2_1^+)$, we extract a $B(E2)$ consistent with that from Ref. [21]. This highlights the risks in using Coulomb-excitation data to determine $B(E2)$

values without appropriate constraints on strongly correlated matrix elements.

$B(E2; 0_1^+ \to 2_1^+)$ and $Q_s(2_1^+)$ values in krypton isotopes are shown in Fig. 6, including the presently determined results. Also shown are the spectroscopic quadrupole moments expected from an axially symmetric prolate rotor, which can be calculated based on the measured $B(E2; 0_1^+ \to 2_1^+)$ to be

$$Q_s(2_1^+) = -\frac{2}{7}\sqrt{\frac{16\pi}{5} B(E2; 0_1^+ \to 2_1^+)}. \tag{1}$$

TABLE IV. Matrix elements for ^{82}Kr as determined in the present work, compared to literature data, where available. Systematic uncertainties, where significant, are quoted as a second uncertainty.

|	This work		Literature		
^{82}Kr					
$J_i^\pi \to J_f^\pi$	$\langle J_i^\pi \| E2 \| J_f^\pi \rangle$ [eb]	$B(E2; J_i^\pi \to J_f^\pi)$ [e^2fm^4]	$\langle J_i^\pi \| E2 \| J_f^\pi \rangle$ [eb]	$B(E2; J_i^\pi \to J_f^\pi)$ [e^2fm^4]	Ref.
$0_1^+ \to 2_1^+$	0.504(8)(3)	2537(80)(31)	0.474(10)	2245(95)	[15]
$0_1^+ \to 2_2^+$	0.0330(12)(1)	10.9(8)(1)			
$2_1^+ \to 2_2^+$	0.252(9)(1)	127(9)(1)	≈ 0.27	≈ 146	[15]
$2_1^+ \to 4_1^+$	0.74(7)(1)	1092(211)(31)	$0.78\binom{22}{31}$	1219(770)	[15]
$J_i^\pi \to J_f^\pi$	$\langle J_i^\pi \| M1 \| J_f^\pi \rangle$ [μ_N]	$B(M1; J_i^\pi \to J_f^\pi)$ [μ_N^2]	$\langle J_i^\pi \| M1 \| J_f^\pi \rangle$ [μ_N]	$B(M1; J_i^\pi \to J_f^\pi)$ [μ_N^2]	Reference
$2_1^+ \to 2_2^+$	0.073(9)(1)	0.0011(2)(3)	≈ 0.075	≈ 0.0011	[15]
	$\langle J_i^\pi \| E2 \| J_i^\pi \rangle$ [eb]	$Q_s(J^\pi)$ [$e$fm^2]	$\langle J_i^\pi \| E2 \| J_i^\pi \rangle$ [eb]	$Q_s(J^\pi)$ [$e$fm^2]	Reference
2_1^+	$-0.33(8)(6)$	$-25(6)(4)$			
4_1^+	0.04(75)	3(57)			
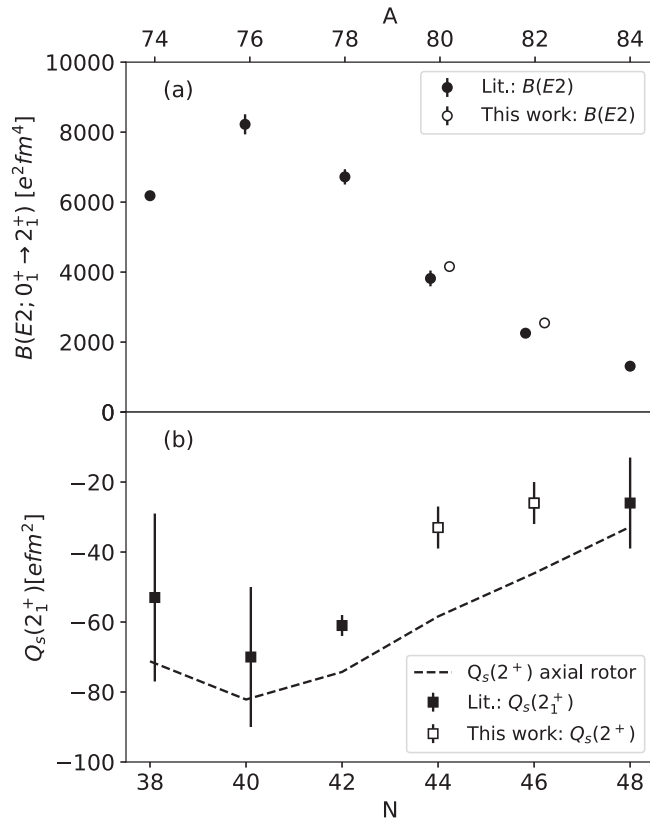
FIG. 6. $B(E2; 0_1^+ \rightarrow 2_1^+)$ and $Q_s(2_1^+)$ values in isotopes of krypton, with the present results indicated. Also shown are the $Q_s(2_1^+)$ values expected for an axially symmetric rotor, as described in Eq. (1). Literature data taken from Ref. [15].
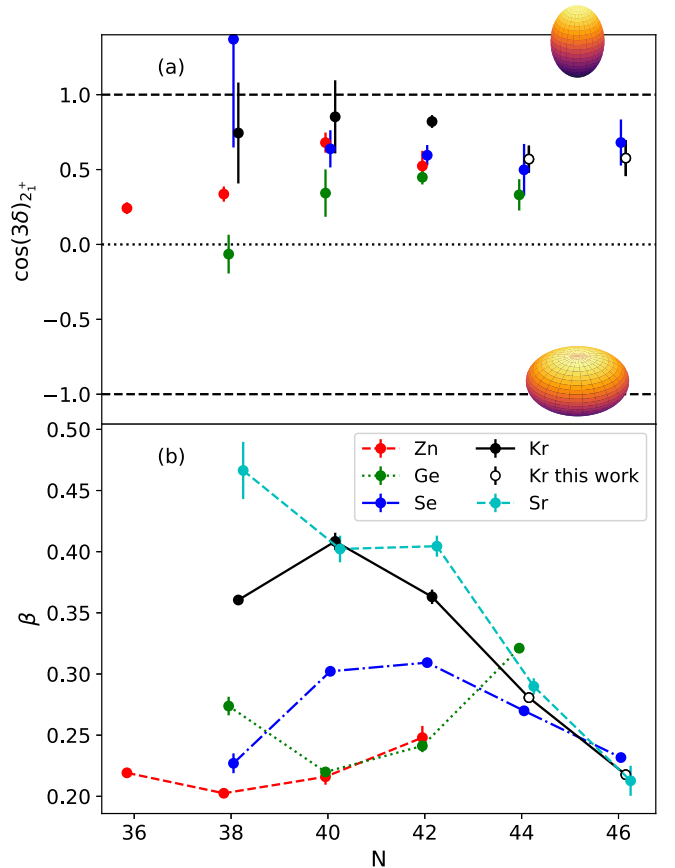

FIG. 7. (a) $\cos(3\delta)_{2_1^+}$ as defined in Eq. (2) for isotopes of Zn, Ge, Se, and Kr. A value of 1 corresponds to an axially symmetric prolate central deformation, -1 to an axially symmetric oblate central deformation and 0 to a central maximally triaxial configuration. It can be seen that isotopes of krypton are approaching the axially symmetric prolate limit. (b) β values, as calculated using Eq. (3) for the same isotopes, as well as for isotopes of strontium. The β values are seen to systematically increase towards a maximum in the strontium and krypton isotopes. ^{72}Zn values taken from Ref. [28] and ^{76,78}Sr values from the weighted average presented in Ref. [2], all other literature values from Ref. [15].

Sum rules, as defined in Refs. [22,23] can be used to provide a model-independent determination of the nuclear shape through rotationally invariant quantities. Recent examples of such analyses can be found in Refs. [24–26]. Within the invariant scheme, one can define charge analogs of the β and γ parameters of the Bohr Hamiltonian. Here, β defines the magnitude of the deformation, while γ relates to the form of the deformation with $\gamma = 0°$ corresponding to an axial prolate shape, $\gamma = 60°$ an axial oblate shape and $\gamma = 30°$ to a maximally triaxial shape. The charge analogs of these parameters are denoted Q and δ for β and γ, respectively. One approximate relation [27] that can be derived from the invariant sum rules is

$$\cos(3\delta) \approx \cos(3\delta)_{2_1^+} = -\frac{Q_s(2_1^+)}{\frac{2}{7}\sqrt{\frac{16\pi}{5} \times B(E2; 0_1^+ \rightarrow 2_1^+)}}, \quad (2)$$

corresponding to the ratio of observed and predicted $Q_s(2_1^+)$ values, as given in Eq. (1). This approximation amounts to the solution for $\cos(3\delta)$ when only contributions from the first 2^+ state are included in the invariant sum rules of Refs. [22,23]. Under the assumption that matter and charge distributions are equivalent (i.e., $\delta = \gamma$), this relation yields the expectation value for the Bohr γ parameter, providing an indication of the central nuclear shape. Importantly, it provides no indication of the so-called "softness" of the nuclear shape, and should

therefore be treated with care when attempting to provide a complete description of deformation. Additionally, as described in Ref. [27], the approximate nature of the relation in Eq. (2) could be associated with an uncertainty (due to an incomplete subset of matrix elements) of $\sigma(\cos(3\delta)) \approx 0.26$. Nonetheless, a systematic analysis of $\cos(3\delta)_{2_1^+}$ values allows for the understanding of how the form of the nuclear shape evolves from, e.g., centrally triaxial deformations towards centrally axial deformations.

The top panel of Fig. 7 shows $\cos(3\delta)_{2_1^+}$ for isotopes of zinc, germanium, selenium, and krypton. It can be seen that, with the exception of ^{72}Se which has large uncertainty [29], ^{74,76,78}Kr provide the closest description to (prolate) axial symmetry at their respective neutron numbers, while ^{80,82}Kr behave similarly to their selenium isotones. Plotted in the bottom panel of Fig. 7 is the Bohr β parameter, calculated

as

$$\beta = \frac{4\pi}{3ZR_0^2}\sqrt{\frac{B(E2; 0_1^+ \rightarrow 2_1^+)}{e^2}}, \qquad (3)$$

where e is the elementary charge, Z is the atomic number, and $R_0 = 1.2A^{1/3}$ fm, with A as the mass number. This shows the behavior of the absolute degree of quadrupole deformation within each isotopic chain.

Viewed in combination, the top and bottom panels of Fig. 7 begin to paint a picture of evolving shapes approaching $N = Z = 40$. In germanium isotopes the influence of the $N = 40$ subshell closure remains strong, resulting in a minimum for β. Moving into the selenium isotopic chain, the influence of the $N = 40$ closure appears to be weakening and the trend in β moves towards a more traditional midshell pattern. This is reflected in the $\cos(3\delta)_{2_1^+}$ values, which tend away from triaxial values, especially for $N \leqslant 42$. Reaching krypton, the results from the present work show a similar structure in the $N = 44, 46$ isotopes as for their selenium isotones. For $N \leqslant 42$ however a dramatic change occurs, with β values increasing significantly and $\cos(3\delta)_{2_1^+}$ values (albeit with large uncertainties for ^{74,76}Kr) now approaching values consistent with axial prolate deformation. Clearly, any sphericity-driving influence on the ground-state deformation from the $N = 40$ subshell closure has dramatically diminished. One might expect that neutron-deficient strontium isotopes approach axial prolate deformation around $N = 40$, completing the collapse in influence of the $N = 40$ subshell closure.

The advantage of the above analysis is its simplicity, requiring only $B(E2; 0_1^+ \rightarrow 2_1^+)$ and $Q_s(2_1^+)$ values and can therefore being applicable for multiple nuclei in the region. In the case of ^{80}Kr, the present data allow for a more detailed calculation of rotational invariants, incorporating $E2$ matrix elements coupled to the 2_2^+ state. For completeness, we here define the first two rotational invariants, reminding the reader that Q can be considered a charge analog of β and δ a charge analog of the γ parameter. For a state of interest, s,

$$\langle s|\hat{Q}^2|s\rangle = \sqrt{5}\langle s|[\hat{E}2 \times \hat{E}2]_0|s\rangle \qquad (4)$$

and

$$\langle s|\widehat{Q^3 \cos(3\delta)}|s\rangle = -\frac{\sqrt{35}}{\sqrt{2}}\langle s|\{[\hat{E}2 \times \hat{E}2]_2 \times \hat{E}2\}_0|s\rangle. \qquad (5)$$

Through an intermediate state expansion, and using the shorthand $M_{if} = \langle i|\hat{E}2|f\rangle$,

$$\langle s|[\hat{E}2 \times \hat{E}2]_0|s\rangle = \frac{(-1)^{2I_s}}{\sqrt{(2I_s+1)}}\sum_t M_{st}M_{ts}\begin{Bmatrix} 2 & 2 & 0 \\ I_s & I_s & I_t \end{Bmatrix} \qquad (6)$$

and

$$\langle s|\{[\hat{E}2 \times \hat{E}2]_2 \times \hat{E}2\}_0|s\rangle$$
$$= \frac{(-1)^{2I_s}}{2I_s+1}\sum_{tu} M_{su}M_{ut}M_{ts}\begin{Bmatrix} 2 & 2 & 2 \\ I_s & I_t & I_u \end{Bmatrix}, \qquad (7)$$

where $\{...\}$ correspond to Wigner-$6j$ symbols.

The invariants were calculated by drawing 1×10^6 samples from the multivariate normal distribution defined by the
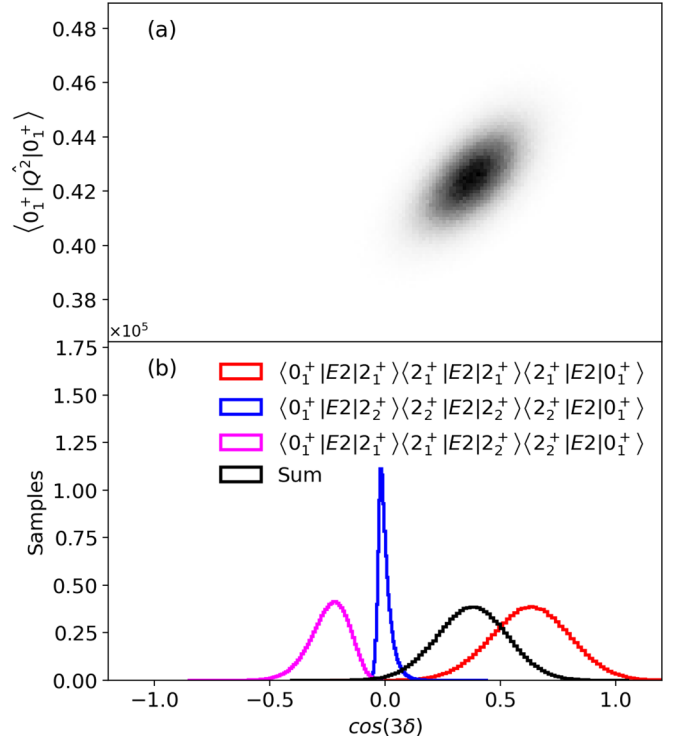

FIG. 8. (a) $\langle 0_1^+|\hat{Q}^2|0_1^+\rangle$ plotted against $\cos(3\delta)$ in ^{80}Kr, calculated with samples drawn from the multivariate normal distribution defined by the mean values from the fitted matrix elements in Table III and the covariance matrix extracted from the fit (Table VI). See text for details of the calculation of the Q^2 and $\cos(3\delta)$ values. (b) Contributions to $\cos(3\delta)$ from matrix element products.

mean parameter values and the covariance matrix in order to account for correlations between measured matrix elements. Figure 8 shows the resultant distribution for the Q^2 invariant (the charge analog of β^2) and $\cos(3\delta)$, which is calculated

TABLE V. Contributions to the values of $\langle\hat{Q}^2\rangle$, $\langle\widehat{Q^3 \cos(3\delta)}\rangle$, and $\cos(3\delta)$ determined in the present work, separated by matrix element product. The sum values correspond to the sum of all contributions. In the case of $\cos(3\delta)$, the summed value of $\langle\hat{Q}^2\rangle$ was used in the denominator of Eq. (8) for all contributions.

$\langle s|\hat{E}2|t\rangle\langle t|\hat{E}2|s\rangle$	$\langle 0_1^+|\hat{Q}^2|0_1^+\rangle$ (e^2b^2)
$\langle 0_1^+|\hat{E}2|2_1^+\rangle\langle 2_1^+|\hat{E}2|0_1^+\rangle$	0.419(13)
$\langle 0_1^+|\hat{E}2|2_2^+\rangle\langle 2_2^+|\hat{E}2|0_1^+\rangle$	0.006(23)
Sum	0.425(13)
$\langle s|\hat{E}2|u\rangle\langle u|\hat{E}2|t\rangle\langle t|\hat{E}2|s\rangle$	$\langle\widehat{Q^3 \cos(3\delta)}\rangle$ (e^{3}b^3)
$\langle 0_1^+|\hat{E}2|2_1^+\rangle\langle 2_1^+|\hat{E}2|2_1^+\rangle\langle 2_1^+|\hat{E}2|0_1^+\rangle$	0.171(50)
$\langle 0_1^+|\hat{E}2|2_2^+\rangle\langle 2_2^+|\hat{E}2|2_2^+\rangle\langle 2_2^+|\hat{E}2|0_1^+\rangle$	−0.0002(81)
$\langle 0_1^+|\hat{E}2|2_1^+\rangle\langle 2_1^+|\hat{E}2|2_2^+\rangle\langle 2_2^+|\hat{E}2|0_1^+\rangle$	−0.065(23)
Sum	0.106(45)
$\langle s|\hat{E}2|u\rangle\langle u|\hat{E}2|t\rangle\langle t|\hat{E}2|s\rangle$	$\cos(3\delta)$
$\langle 0_1^+|\hat{E}2|2_1^+\rangle\langle 2_1^+|\hat{E}2|2_1^+\rangle\langle 2_1^+|\hat{E}2|0_1^+\rangle$	0.630(169)
$\langle 0_1^+|\hat{E}2|2_2^+\rangle\langle 2_2^+|\hat{E}2|2_2^+\rangle\langle 2_2^+|\hat{E}2|0_1^+\rangle$	−0.001(30)
$\langle 0_1^+|\hat{E}2|2_1^+\rangle\langle 2_1^+|\hat{E}2|2_2^+\rangle\langle 2_2^+|\hat{E}2|0_1^+\rangle$	−0.242(85)
Sum	0.378(153)

from the first and second rotational invariants under the assumption that

$$\cos(3\delta) = \frac{\langle 0_1^+ | \widehat{Q^3 \cos(3\delta)} | 0_1^+ \rangle}{\langle 0_1^+ | \hat{Q}^2 | 0_1^+ \rangle^{3/2}}. \tag{8}$$

Also shown in Fig. 8 are the contributions to the $\cos(3\delta)$ value from the individual matrix element products, which are summarized in Table V. Note that the sum Q^2 value was used to calculate $\cos(3\delta)$ for the individual contributions given in Table V and Fig. 8. The result of this analysis is a reduced value of $\cos(3\delta)$ as compared to that determined from Eq. (2), though the central value remains predominantly prolate.

We briefly now compare the present results with some recent theoretical calculations. In Ref. [30] symmetry-conserving configuration-mixing methods were used with the Gogny D1S interaction to study the krypton isotopic chain. In these calculations, the ground-state collective wave functions for ^{74,76,78}Kr were found to be predominantly prolate—approaching an axial configuration in ^{74}Kr. ^{80,82}Kr, on the other hand, were found to have ground-state collective wave functions with a slightly oblate configuration, albeit one that is rather closer to maximal triaxiality than in the ^{74,76,78}Kr cases. This is born out in the calculated $Q_s(2_1^+)$ values, which are negative for ^{74,76,78}Kr and positive in ^{80,82}Kr. This discrepancy for ^{80,82}Kr should not be overstated: the potential energy surfaces for both isotopes in the calculations of Ref. [30] are not rigid in the γ degree of freedom. Significant components of the collective wave functions span the line of $\gamma = 30°$, corresponding to maximal triaxiality and distinguishing prolate and oblate deformations.

IV. CONCLUSIONS

We presented the first determination of the spectroscopic quadrupole moments for the first 2^+ states, $Q(2_1^+)$, in ^{80,82}Kr following Coulomb excitation on high-Z targets. Target normalization allowed for $E2$ matrix elements to be extracted independent of the literature values. Nine matrix elements are

newly determined in the present work, while six are extracted with improved precision.

An analysis of rotational invariants in ^{80}Kr incorporating matrix elements coupled to the 2_2^+ state results in a reduced $\cos(3\delta)$ value, albeit still consistent with a dominantly prolate central deformation. A systematic comparison of invariants incorporating higher lying states is hindered by the varying quality and availability of the experimental data: genuine physical effects and missing experimental data might easily by confused.

Instead, a simpler parametrization of the triaxial degree of freedom was employed, using only the $B(E2; 0_1^+ \rightarrow 2_1^+)$ and $Q_s(2_1^+)$ values. This allowed for a comparison of experimental data in Zn, Ge, Se, and Kr isotopes, indicating a trend towards axial symmetry in the Kr isotopes with $N \leqslant 42$. Improved measurements of ^{74,76}Kr will be essential to confirming this evolution. Looking beyond the krypton isotopes, if this evolution continues for higher-Z nuclei, one might expect that neutron-deficient Sr and Zr isotopes approach axial prolate deformation in their ground states.

APPENDIX

For completeness, we report covariances and correlations on matrix elements for ^{80}Kr and ^{82}Kr in Tables VI and VII, respectively.

TABLE VI. Variances (bold, diagonal), covariances (above diagonal) and correlations (below diagonal) arising from the fit of ^{80}Kr. Mean values, μ are given in units of eb for $E2$ matrix elements and μ_N for $M1$ matrix elements.

$\langle J_i^\pi \| E\lambda \| J_f^\pi \rangle$	μ	$\langle 0_1^+\|E2\|2_1^+ \rangle$	$\langle 0_1^+\|E2\|2_2^+ \rangle$	$\langle 2_1^+\|E2\|2_1^+ \rangle$	$\langle 2_1^+\|E2\|2_2^+ \rangle$	$\langle 2_1^+\|E2\|0_2^+ \rangle$	$\langle 2_1^+\|E2\|4_1^+ \rangle$	$\langle 2_2^+\|E2\|2_2^+ \rangle$	$\langle 2_2^+\|E2\|0_2^+ \rangle$	$\langle 4_1^+\|E2\|4_1^+ \rangle$	$\langle 4_1^+\|E2\|6_1^+ \rangle$	$\langle 2_1^+\|M1\|2_2^+ \rangle$
$\langle 0_1^+\|E2\|2_1^+ \rangle$	0.6449	**4.3×10^{-5}**	-1.0×10^{-5}	-9.0×10^{-5}	-8.9×10^{-5}	1.5×10^{-4}	-8.1×10^{-6}	1.7×10^{-3}	-7.4×10^{-4}	6.8×10^{-5}	-6.2×10^{-7}	-7.8×10^{-6}
$\langle 0_1^+\|E2\|2_2^+ \rangle$	0.0782	-0.106	**2.2×10^{-4}**	-3.1×10^{-4}	2.0×10^{-3}	-1.4×10^{-3}	5.6×10^{-5}	-2.3×10^{-2}	8.1×10^{-3}	-1.5×10^{-3}	-7.8×10^{-5}	1.7×10^{-4}
$\langle 2_1^+\|E2\|2_1^+ \rangle$	-0.4339	-0.189	-0.287	**5.3×10^{-3}**	-3.0×10^{-3}	-2.8×10^{-4}	-2.3×10^{-4}	1.8×10^{-2}	-1.5×10^{-4}	2.5×10^{-3}	3.5×10^{-4}	-2.5×10^{-4}
$\langle 2_1^+\|E2\|2_2^+ \rangle$	0.7327	-0.098	0.984	-0.299	**1.9×10^{-2}**	-1.3×10^{-2}	5.3×10^{-4}	-0.22	7.7×10^{-2}	-1.4×10^{-2}	-7.4×10^{-4}	1.6×10^{-3}
$\langle 2_1^+\|E2\|0_2^+ \rangle$	0.3346	0.193	-0.811	-0.033	-0.821	**1.3×10^{-2}**	-4.5×10^{-4}	0.19	-7.2×10^{-2}	1.3×10^{-2}	1.7×10^{-3}	-1.1×10^{-3}
$\langle 2_1^+\|E2\|4_1^+ \rangle$	1.0693	-0.041	0.125	-0.104	0.127	-0.130	**9.2×10^{-4}**	-7.1×10^{-3}	2.6×10^{-3}	-4.6×10^{-3}	-4.5×10^{-4}	4.5×10^{-5}
$\langle 2_2^+\|E2\|2_2^+ \rangle$	0.4467	0.148	-0.929	0.148	-0.944	0.952	-0.138	**2.9**	-1.1	0.19	1.9×10^{-2}	-1.9×10^{-2}
$\langle 2_2^+\|E2\|0_2^+ \rangle$	-0.0796	-0.178	0.861	-0.033	0.872	-0.98	0.133	-0.981	**0.40**	-6.8×10^{-2}	-8.3×10^{-3}	6.5×10^{-3}
$\langle 4_1^+\|E2\|4_1^+ \rangle$	-0.7661	0.048	-0.475	0.160	-0.481	0.505	-0.698	0.518	-0.492	**4.7×10^{-2}**	-3.7×10^{-3}	-1.2×10^{-3}
$\langle 4_1^+\|E2\|6_1^+ \rangle$	1.6809	-0.0008	-0.045	0.042	-0.046	0.131	-0.130	0.098	-0.113	-0.148	**1.3×10^{-2}**	-6.5×10^{-5}
$\langle 2_1^+\|M1\|2_2^+ \rangle$	0.0654	-0.075	0.732	-0.217	0.726	-0.602	0.093	-0.689	0.638	-0.353	-0.035	**2.5×10^{-4}**

TABLE VII. Variances (bold, diagonal), covariances (above diagonal) and correlations (below diagonal) arising from the fit of ^{82}Kr. Mean values, μ are given in units of eb for $E2$ matrix elements and μ_N for $M1$ matrix elements.

$\langle J_i^\pi \vert E\lambda \vert J_f^\pi \rangle$	μ	$\langle 0_1^+ \vert E2 \vert 2_1^+ \rangle$	$\langle 0_1^+ \vert E2 \vert 2_2^+ \rangle$	$\langle 2_1^+ \vert E2 \vert 2_1^+ \rangle$	$\langle 2_1^+ \vert E2 \vert 2_2^+ \rangle$	$\langle 2_1^+ \vert E2 \vert 4_1^+ \rangle$	$\langle 4_1^+ \vert E2 \vert 4_1^+ \rangle$	$\langle 2_1^+ \vert M1 \vert 2_2^+ \rangle$
$\langle 0_1^+ \vert E2 \vert 2_1^+ \rangle$	0.5037	**6.2×10^{-5}**	-3.4×10^{-7}	-3.7×10^{-4}	2.6×10^{-6}	6.6×10^{-5}	-9.2×10^{-4}	-7.2×10^{-6}
$\langle 0_1^+ \vert E2 \vert 2_2^+ \rangle$	0.0330	-0.369	**1.4×10^{-6}**	5.1×10^{-7}	8.9×10^{-6}	-1.4×10^{-5}	1.8×10^{-4}	5.4×10^{-6}
$\langle 2_1^+ \vert E2 \vert 2_1^+ \rangle$	-0.3295	-0.601	-0.006	**6.0×10^{-3}**	-5.6×10^{-5}	-1.5×10^{-3}	1.5×10^{-2}	7.4×10^{-5}
$\langle 2_1^+ \vert E2 \vert 2_2^+ \rangle$	0.2522	0.039	0.862	-0.083	**7.5×10^{-5}**	4.7×10^{-5}	-1.6×10^{-4}	1.4×10^{-5}
$\langle 2_1^+ \vert E2 \vert 4_1^+ \rangle$	0.7391	0.119	-0.164	-0.276	-0.076	**5.1×10^{-3}**	-3.9×10^{-2}	-2.2×10^{-4}
$\langle 4_1^+ \vert E2 \vert 4_1^+ \rangle$	0.0398	-0.186	0.243	0.299	-0.029	-0.860	**0.393**	2.3×10^{-3}
$\langle 2_1^+ \vert M1 \vert 2_2^+ \rangle$	0.0728	-0.133	0.666	0.138	0.228	-0.444	0.528	**4.7×10^{-5}**

[1] A. Poves, F. Nowacki, and Y. Alhassid, Phys. Rev. C **101**, 054307 (2020).

[2] R. D. O. Llewellyn, M. A. Bentley, R. Wadsworth, H. Iwasaki, J. Dobaczewski, G. de Angelis, J. Ash, D. Bazin, P. C. Bender, B. Cederwall, B. P. Crider, M. Doncel, R. Elder, B. Elman, A. Gade, M. Grinder, T. Haylett, D. G. Jenkins, I. Y. Lee, B. Longfellow *et al.*, Phys. Rev. Lett. **124**, 152501 (2020).

[3] T. R. Rodríguez and J. L. Egido, Phys. Lett. B **705**, 255 (2011).

[4] E. Clément, A. Görgen, W. Korten, E. Bouchez, A. Chatillon, J.-P. Delaroche, M. Girod, H. Goutte, A. Hürstel, Y. LeCoz, A. Obertelli, S. Péru, C. Theisen, J. N. Wilson, M. Zielińska, C. Andreoiu, F. Becker, P. A. Butler, J. M. Casandjian, W. N. Catford *et al.*, Phys. Rev. C **75**, 054313 (2007).

[5] F. Becker, A. Petrovici, J. Iwanicki, N. Amzal, W. Korten, K. Hauschild, A. Hurstel, C. Theisen, P. Butler, R. Cunningham, T. Czosnyka, G. de France, J. Gerl, P. Greenlees, K. Helariutta, R.-D. Herzberg, P. Jones, R. Julin, S. Juutinen, H. Kankaanpää *et al.*, Nucl. Phys. A **770**, 107 (2006).

[6] E. Lunderberg, J. Belarge, P. Bender, B. Bucher, D. Cline, B. Elman, A. Gade, S. Liddick, B. Longfellow, C. Prokop, D. Weisshaar, and C. Wu, Nucl. Instrum. Methods Phys. Res. A **885**, 37 (2018).

[7] K. Jayamanna *et al.*, Rev. Sci. Instrum. **79**, 02C711 (2008).

[8] Micron Semiconductor Ltd., Micron catalog, (2019).

[9] G. Hackman and C. E. Svensson, Hyperfine Int. **225**, 241 (2014).

[10] https://github.com/GRIFFINCollaboration/GRSISort/.

[11] R. Brun and F. Rademakers, Nucl. Instrum. Methods Phys. Res. A **389**, 81 (1997).

[12] T. Czosnyka, D. Cline, and C. Y. Wu, Bull. Am. Phys. Soc. **28**, 745 (1983).

[13] F. James, MINUIT function minimization and error analysis (1994).

[14] M. Zielińska, L. P. Gaffney, K. Wrzosek-Lipska, E. Clément, T. Grahn, N. Kesteloot, P. Napiorkowski, J. Pakarinen, P. Van Duppen, and N. Warr, Eur. Phys. J. A **52**, 99 (2016).

[15] NNDC, Evaluated Nuclear Structure Data File (ENSDF).

[16] C. Lim, R. Spear, M. Fewell, and G. Gyapong, Nucl. Phys. A **548**, 308 (1992).

[17] K. Krane, Appl. Radiat. Isot. **69**, 201 (2011).

[18] L. Funke, J. Döring, F. Dubbers, P. Kemnitz, E. Will, G. Winter, V. Kiptilij, M. Kudojarov, I. Lemberg, A. Pasternak, A. Mishin, L. Hildingsson, A. Johnson, and T. Lindblad, Nucl. Phys. A **355**, 228 (1981).

[19] H. G. Friederichs, A. Gelberg, B. Heits, K. P. Lieb, M. Uhrmacher, K. O. Zell, and P. von Berntano, Phys. Rev. Lett. **34**, 745 (1975).

[20] T. J. Mertzimekis, N. Benczer-Koller, J. Holden, G. Jakob, G. Kumbartzki, K.-H. Speidel, R. Ernst, A. Macchiavelli, M. McMahan, L. Phair, P. Maier-Komor, A. Pakou, S. Vincent, and W. Korten, Phys. Rev. C **64**, 024314 (2001).

[21] J. Keinonen, K. P. Lieb, H. P. Hellmeister, A. Bockisch, and H. Emling, Nucl. Phys. A **376**, 246 (1982).

[22] K. Kumar, Phys. Rev. Lett. **28**, 249 (1972).

[23] D. Cline, Annu. Rev. Nucl. Part. Sci. **36**, 683 (1986).

[24] L. Morrison, K. Hadyńska-Klęk, Z. Podolyák, D. T. Doherty, L. P. Gaffney, L. Kaya, L. Próchniak, J. Samorajczyk-Pyśk, J. Srebrny, T. Berry, A. Boukhari, M. Brunet, R. Canavan, R. Catherall, S. J. Colosimo, J. G. Cubiss, H. De Witte, C. Fransen, E. Giannopoulos, H. Hess *et al.*, Phys. Rev. C **102**, 054304 (2020).

[25] J. Henderson, C. Y. Wu, J. Ash, B. A. Brown, P. C. Bender, R. Elder, B. Elman, A. Gade, M. Grinder, H. Iwasaki, B. Longfellow, T. Mijatović, D. Rhodes, M. Spieker, and D. Weisshaar, Phys. Rev. C **99**, 054313 (2019).

[26] K. Hadyńska-Klęk, P. J. Napiorkowski, M. Zielińska, J. Srebrny, A. Maj, F. Azaiez, J. J. Valiente Dobón, M. Kicińska Habior, F. Nowacki, H. Naïdja, B. Bounthong, T. R. Rodríguez, G. de Angelis, T. Abraham, G. Anil Kumar, D. Bazzacco, M. Bellato, D. Bortolato, P. Bednarczyk, G. Benzoni *et al.*, Phys. Rev. C **97**, 024326 (2018).

[27] J. Henderson, Phys. Rev. C **102**, 054306 (2020).

[28] S. Hellgartner, Probing Nuclear Shell Structure beyond the N = 40 Subshell using Multiple Coulomb Excitation and Transfer Experiments, Ph.D. thesis, Technischen Universität München (2015).

[29] J. Henderson, C. Y. Wu, J. Ash, P. C. Bender, B. Elman, A. Gade, M. Grinder, H. Iwasaki, E. Kwan, B. Longfellow, T. Mijatović, D. Rhodes, M. Spieker, and D. Weisshaar, Phys. Rev. Lett. **121**, 082502 (2018).

[30] T. R. Rodríguez, Phys. Rev. C **90**, 034306 (2014).